Plasma modeling for a nonsymmetric capacitive discharge driven by a nonsinusoidal radio frequency current

M. N. A. Dewan and P. J. McNally[a)]
Microelectronics Research Laboratory, Research Institute for Networks and Communications Engineering (RINCE), School of Electronic Engineering, Dublin City University, Dublin 9, Ireland

P. A. F. Herbert
Plasma Ireland Ltd., 22 Summerhill North, Cork, Ireland

(Received 25 January 2002; accepted for publication 28 January 2002)

An analytical solution for the sheath dynamics of an asymmetrically driven capacitively coupled plasma is obtained under the assumptions of time-independent, collisionless ion motion, inertialess electrons, and uniform current density. Modeling is performed considering that the plasma is driven by a nonsinusoidal radio frequency (rf) current which can be resolved into a finite number of harmonic components. Together with different sheath parameters the equation for the bulk plasma impedance is also obtained to calculate the overall plasma impedance and the overall rf voltage. Assuming equal plate areas the solution for a symmetric discharge is also obtainable from this model. We have found that the even harmonic components of rf voltage and impedance are always present, even in a symmetric discharge. Experimental results are shown to be in qualitative agreement with the theoretical model. The values of normalized rf voltage and impedance harmonics assume lower values as the asymmetry of the plasma chamber decreases. © *2002 American Institute of Physics.* [DOI: 10.1063/1.1462425]

I. INTRODUCTION

Capacitively coupled radio-frequency (rf) plasmas play an important role in a number of material processing applications in the microelectronics industry.[1] In such a discharge the electrons can be thought of as oscillating back and forth between the two electrodes, with most of the applied voltage dropped across the sheaths near the electrodes. The motion of the sheath boundaries is highly nonlinear. Various authors have developed models to account for the electron and ion dynamics within the sheaths.[2–16] However, the nonlinear ion and electron dynamics are not treated self-consistently within these models. Lieberman developed an analytical, self-consistent solution for the collisionless rf sheath considering a single sinusoidal rf current.[17] This model was based on a symmetrically driven (equal-area plates), parallel plate rf discharge. The effect of asymmetrical sizes of the two plates was not considered in the Lieberman model. In reality most reactors used for plasma processing are asymmetrical,[18] where the powered electrode area is smaller than the grounded electrode area. Again, due to the complex behavior of the plasma sheaths, the driving rf current always contains some harmonics[19,20] which contribute significantly to each of the plasma parameters. To date little work has been carried out on the analysis of the behavior of the sheath beyond the fundamental frequency of the rf current.

In this work we have developed an analytical solution for a collisionless rf sheath considering a nonsymmetric capacitive discharge and all harmonic components of the rf current. We obtain expressions for the time-averaged ion and electron densities, electric field and electric potential within the sheath, nonlinear oscillation motion of the electron sheath boundary, nonlinear oscillating sheath voltage, and the effective sheath impedance. Finally, we have included the impedance of the bulk plasma to determine the overall impedance and the overall rf voltage between the two plates. Assuming equal plate areas it is also possible to obtain solutions for the symmetrical discharge from this model. For the calculation of different parameters a comparison is made with the Lieberman model.[17]

II. MODELING OF RF PLASMA

In the following model we assume that the current density at a particular distance from either of the plates is uniform throughout the cross section of the plasma.

A. Analysis of plasma sheath

In the sheath analysis all the assumptions made in the Lieberman model[17] are also assumed to be valid in this model except that the driving rf current is assumed to be no longer sinusoidal in nature. We assume that the rf current is nonsinusoidal but it can be resolved into a finite number of harmonic components whose frequencies are integer multiples of the driving frequency. This is a good approximation when the current is periodic in nature in time space and the magnitude of harmonic components at very high frequencies is very small compared to the fundamental and can be neglected. The structure of the rf sheath is shown in Fig. 1. Ions crossing the ion sheath boundary at $x=0$ accelerate within the sheath and strike the electrode at $x=s_m$ with high energies. The ion density is sketched as the heavy, solid line in Fig. 1. The nonsinusoidal rf current can be expressed as a

[a)]Electronic mail: mcnallyp@eeng.dcu.ie

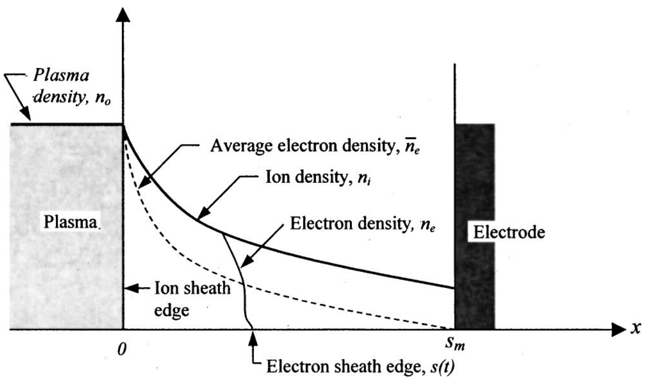

FIG. 1. Structure of the high voltage, capacitive rf sheath. Ions crossing the ion sheath boundary at $x=0$ accelerate within the sheath and strike the electrode at $x=s_m$.

summation of several sinusoidal harmonic components which flow along the x axis through the sheath and can be written as[21]

$$J_{\mathrm{rf}}(t)=-\sum_{p=1}^{N}\overline{J_p}\sin(p\omega t),\tag{1}$$

where $J_p(t)=-\overline{J_p}\sin(p\omega t)$ is the pth harmonic component of rf current density. $\overline{J_p}$ and ω are the amplitude of the pth harmonic current density and the angular frequency of the fundamental component of rf current, respectively.

In the derivation of the sheath parameters we followed the same procedure as described in the Lieberman model[17] except that the sinusoidal current density used in Lieberman's equations is replaced by the nonsinusoidal current density given by Eq. (1). Thus the sheath parameters obtained in this model are given by the equations below. Their derivation is included in Appendix A. Most of the following equations contain one or more integration operations. The results after the integrations are not shown for simplicity as the results are quite complicated.

Given the results of Appendix A, the time-average electron density can now be obtained by Eq. (A4). Differentiating Eq. (A12), using Eqs. (A1) and (A14), and equating $d\overline{E}/dx=\rho/\varepsilon_0$ we obtain the net charge density as

$$\rho=\frac{\varphi}{\pi}n_i e.\tag{2}$$

Note that the equations for the time-average electron density and the charge density are the same as in the Lieberman model[17] except that the ion density n_i used in Eqs. (A4) and (2) is given by Eq. (A18).

Integrating the instantaneous electric field given by Eq. (A10) with respect to x, we obtain the instantaneous voltage $V(t)$ from the plasma to the electrode across the sheath as

$$\begin{aligned}V(t)&=\int_s^{s_m}E(x,t)dx\\&=\int_{\omega t}^{\pi}\sum_{p=1}^{N}\frac{\overline{J_p}}{p\omega\varepsilon_0}[\cos(p\omega t)-\cos(p\varphi)]\frac{dx}{d\varphi}d\varphi.\end{aligned}\tag{3}$$

Using Eqs. (A14) and (A15) and inserting into Eq. (3) we obtain the equation for the instantaneous sheath voltage $V(t)$, for $0<\omega t<\pi$, as

$$\begin{aligned}e\omega^2\varepsilon_0 n_0 V(t)=&\int_{\omega t}^{\pi}\sum_{p=1}^{N}\sum_{q=1}^{N}\frac{\overline{J_p}\,\overline{J_q}}{p}\{\cos(p\omega t)-\cos(p\varphi)\}\sin(q\varphi)d\varphi-\frac{1}{e\omega^2T_e\varepsilon_0\pi n_0}\\&\times\int_{\omega t}^{\pi}\Bigg[\sum_{p=1}^{N}\sum_{\substack{q=1\\q\neq p}}^{N}\sum_{r=1}^{N}\sum_{s=1}^{N}\frac{\overline{J_p}\,\overline{J_q}\,\overline{J_r}\,\overline{J_s}}{ps}\Bigg\{\frac{2p+q}{2p(p+q)^2}\sin(p+q)\varphi-\frac{2p-q}{2p(p-q)^2}\sin(p-q)\varphi\\&-\frac{1}{2(p+q)}\varphi\cos(p+q)\varphi+\frac{1}{2(p-q)}\varphi\cos(p-q)\varphi\Bigg\}\{\cos(s\omega t)-\cos(s\varphi)\}\sin(r\varphi)\\&+\sum_{p=1}^{N}\sum_{r=1}^{N}\sum_{s=1}^{N}\frac{J_p^2\overline{J_r}\,\overline{J_s}}{ps}\left\{\frac{3}{8p^2}\sin(2p\varphi)-\frac{\varphi}{4p}\cos(2p\varphi)-\frac{\varphi}{2p}\right\}\times\{\cos(s\omega t)-\cos(s\varphi)\}\sin(r\varphi)d\varphi\Bigg].\end{aligned}\tag{4}$$

$V(t)$ in Eq. (4) is an even, periodic function of ωt with period 2π. For $-\pi<\omega t<0$, $V(t)$ is given by Eq. (4) with ωt in the right-hand side of the equation replaced by $-\omega t$. Expanding $V(t)$ in a Fourier series we have

$$V(t)=\overline{V_0}+\sum_{k=1}^{\infty}\overline{V_k}\cos(k\omega t),\tag{5}$$

where

$$\overline{V_0}=\frac{1}{\pi}\int_0^{\pi}V(\omega t)d\omega t,\tag{6}$$

$$\overline{V_k}=\frac{2}{\pi}\int_0^{\pi}V(\omega t)\cos(k\omega t)d\omega t\quad(k=1,2,3,...).\tag{7}$$

It is evident from Eq. (4) that it is difficult to perform manually the analytical Fourier transforms given by Eqs. (6) and (7). But using a personal computer it is very easy to perform these calculations numerically using any routine programming language, such as FORTRAN, Pascal, C++, etc.

Defining the effective capacitance per unit area using the relation

$$-\overline{J}_k \sin(k\omega t)=C_k\frac{d}{dt}[\overline{V}_k \cos(k\omega t)], \tag{8}$$

we obtain the sheath capacitance (in F/m^2) for the kth harmonic frequency

$$C_k=\frac{\overline{J}_k}{k\omega\overline{V}_k}. \tag{9}$$

From Eq. (A5) we obtain

$$n_s u_s=n_0\sum_{p=1}^{N}\overline{u}_p \sin(p\varphi)=n_0 u_0, \tag{10}$$

where $\overline{u}_p=\overline{J}_p/en_0$ and $u_0=\Sigma_{p=1}^{N}\overline{u}_p \sin(p\varphi)$. From Eqs. (A14) and (A15) we obtain

$$e\omega n_0\frac{dx}{d\varphi}=\sum_{p=1}^{N}\overline{J}_p \sin(p\varphi)-\frac{1}{e\omega^2 T_e\varepsilon_0\pi n_0}\left[\sum_{p=1}^{N}\sum_{\substack{q=1\\ q\neq p}}^{N}\frac{\overline{J}_p\overline{J}_q}{p}\left\{\frac{2p+q}{2p(p+q)^2}\sin(p+q)\varphi-\frac{2p-q}{2p(p-q)^2}\sin(p-q)\varphi\right.\right.$$
$$\left.-\frac{1}{2(p+q)}\varphi\cos(p+q)\varphi+\frac{1}{2(p-q)}\varphi\cos(p-q)\varphi\right\}$$
$$\left.+\sum_{p=1}^{N}\frac{\overline{J}_p^2}{p}\left\{\frac{3}{8p^2}\sin(2p\varphi)-\frac{\varphi}{4p}\cos(2p\sigma)-\frac{\varphi}{2p}\right\}\right]\sum_{p=1}^{N}\overline{J}_p \sin(p\varphi). \tag{11}$$

Using $\varphi=\omega t$ and $u_s=dx/dt$ we obtain from Eq. (11)

$$u_s-u_0=-\frac{1}{e^2\omega^2 T_e\varepsilon_0\pi n_0^2}\left[\sum_{p=1}^{N}\sum_{\substack{q=1\\ q\neq p}}^{N}\frac{\overline{J}_p\overline{J}_q}{p}\left\{\frac{2p+q}{2p(p+q)^2}\sin(p+q)\varphi-\frac{2p-q}{2p(p-q)^2}\sin(p-q)\varphi-\frac{1}{2(p+q)}\varphi\cos(p+q)\varphi\right.\right.$$
$$\left.\left.+\frac{1}{2(p-q)}\varphi\cos(p-q)\varphi\right\}+\sum_{p=1}^{N}\frac{\overline{J}_p^2}{p}\left\{\frac{3}{8p^2}\sin(2p\varphi)-\frac{\varphi}{4p}\cos(2p\varphi)-\frac{\varphi}{2p}\right\}\right]\sum_{p=1}^{N}\overline{J}_p \sin(p\varphi)=F(\varphi). \tag{12}$$

Now, following exactly the same procedure described in the Lieberman model[17] we can write the average stochastic power per unit area for a single sheath as

$$\overline{P}_{\text{stoc}}=\frac{43m}{n_0}\Gamma_s\langle(u_s-u_0)n_s u_s\rangle_\varphi$$
$$=\frac{4m}{\pi n_0}\Gamma_s\int_0^{\pi}(u_s-u_0)n_s u_s d\varphi, \tag{13}$$

where m is the electron mass and for a Maxwellian distribution the incident electron flux Γ_s can be written as[17,22,23]

$$\Gamma_s=\frac{1}{4}n_0\left(\frac{8eT_e}{\pi m}\right)^{1/2}. \tag{14}$$

Inserting Eqs. (10) and (12) into Eq. (13) we obtain

$$\overline{P}_{\text{stoc}}=\frac{4m}{\pi e n_0}\Gamma_s\int_0^{\pi}F(\varphi)\sum_{p=1}^{N}\overline{J}_p \sin(p\varphi)d\varphi. \tag{15}$$

Equation (15) gives the total power dissipated in the plasma sheath by the stochastic heating mechanism. It is evident from Eqs. (12) and (15) that it is impossible to separate the amount of heating corresponding to a particular harmonic component of the rf current. As an approximation we assumed that only the kth harmonic component of rf current is in operation while calculating the stochastic heating corresponding to the kth harmonic frequency. Considering only the kth harmonic component of rf current given by Eq. (1) we have

$$J_k(t)=-\overline{J}_k \sin(k\omega t). \tag{16}$$

Similarly as in Eq. (15), using only the kth harmonic rf current given by Eq. (16) instead of the total current and simplifying, we obtain the average stochastic power for a single sheath per unit area related to only the kth harmonic frequency as

$$\overline{P}_{\text{stoc }k}=\frac{3m\overline{J}_k^4}{8k^2 e^3\omega^2 T_e\varepsilon_0 n_0^3}\Gamma_s, \tag{17}$$

where Γ_s is given by Eq. (14) and $\overline{J}_k$ is the amplitude of the kth harmonic current density. Now, the sheath conductance G_k per unit area for the kth harmonic frequency is defined by the relation[17]

$$\overline{P}_{\text{stoc }k}=\frac{1}{2}\frac{\overline{J}_k^2}{G_k}. \tag{18}$$

Equating (17) and (18) we obtain

$$G_k=\frac{4k^2}{3\overline{J}_k^2}\frac{e^3\omega^2 T_e\varepsilon_0 n_0^3}{m\Gamma_s}. \tag{19}$$

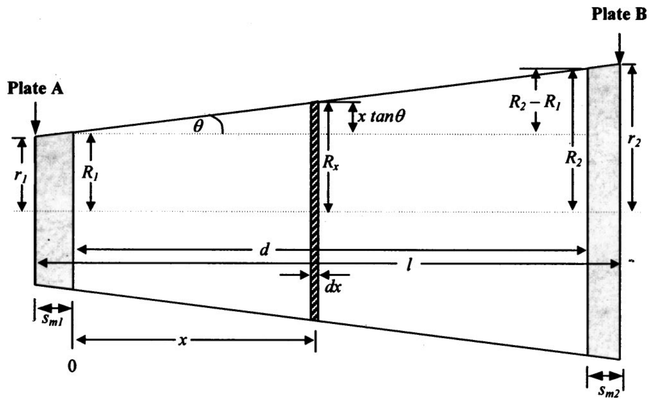

FIG. 2. The schematic diagram of the plasma.

B. Analysis of bulk plasma

In the calculation of the bulk plasma impedance the following assumptions were made.

(a) The plasma outside the two sheaths can be represented as a solid cylinder of length d, with a linearly varying cross-sectional radius from plate A to plate B (Fig. 2).[21]

(b) The plasma density n_0 is inversely proportional to the cross-sectional area of the plasma. This is a good approximation if we assume that the rf current is constant at any distance from either of the plates. Thus the current density becomes inversely proportional to the cross-sectional area and the plasma density increases almost linearly with the current density.[24]

The kth harmonic impedance (ohm) of a bulk plasma slab of thickness dx and cross-sectional area A_x, at a distance x from the ion sheath edge of plate A can be written as[22]

$$dZ_k = \frac{dx}{jk\omega\varepsilon_{px}A_x}, \tag{20}$$

where

$$\varepsilon_{px} = \varepsilon_0\left[1 - \frac{\omega_{pe\ x}^2}{k\omega(k\omega - j\nu_m)}\right]. \tag{21}$$

In this case, the electron plasma frequency

$$\omega_{pe\ x} = \left(\frac{e^2 n_{0x}}{\varepsilon_0 m}\right)^{1/2}, \tag{22}$$

and ν_m = electron-neutral collision frequency. Here n_{0x} is the plasma density at a distance x from the ion sheath edge of plate A, which is also equal to the electron density at that position. From Fig. 2

$$A_x = \pi R_x^2 = \pi(R_1 + x\tan\theta)^2 \tag{23}$$

and

$$\tan\theta = \frac{R_2 - R_1}{d} = \frac{r_2 - r_1}{l}. \tag{24}$$

Here r_1 and r_2 are the radii of the plates A and B, respectively, whereas R_1 and R_2 are the radii of the plasma cylinder at the two ion sheath edges. From Fig. 2 we obtain

$$R_1 = r_1 + s_{m1}\tan\theta, \tag{25}$$

$$R_2 = r_1 + (l - s_{m2})\tan\theta. \tag{26}$$

The effective bulk plasma length d and the separation between the two plates l can be related as

$$d = l - s_{m1} - s_{m2}, \tag{27}$$

where s_{m1} and s_{m2} are the ion sheath thicknesses at plate A and B, respectively. Assuming that the plasma density is inversely proportional to the cross-sectional area of the plasma cylinder we obtain

$$n_{01}A_1 = n_{0x}A_x = n_{02}A_2. \tag{28}$$

The subscripts 1, x, and 2 are used for the positions at the ion sheath edge of plate A, at a distance x from the ion sheath edge of plate A, and at the ion sheath edge of plate B, respectively. Inserting Eqs. (22) and (28) in Eq. (21) we obtain

$$\varepsilon_{px} = \varepsilon_0\left[1 - \frac{e^2 A_1 n_{01}}{k\omega\varepsilon_0 m(k\omega - j\nu_m)A_x}\right]. \tag{29}$$

Using Eqs. (20) and (29) and integrating from $x=0$ to $x=d$ we obtain the kth harmonic bulk impedance as

$$Z_k = \frac{l}{2(r_2 - r_1)d\omega\varepsilon_0\pi}\frac{\sqrt{D_3^2 + D_4^2}}{\sqrt{D_1^2 + D_2^2}}e^{j[\alpha - (\phi/2) - (\pi/2)]}, \tag{30}$$

where ϕ, α, and the coefficients D_i are defined in Appendix B.

Separating the real and imaginary parts of the kth harmonic bulk impedance we can rewrite Eq. (30) as

$$Z_k = Z_{\text{real}} + jZ_{\text{imag}}, \tag{31}$$

where

$$Z_{\text{real}} = \frac{l}{2(r_2 - r_1)k\omega\varepsilon_0\pi}\frac{\sqrt{D_3^2 + D_4^2}}{\sqrt{D_1^2 + D_2^2}}\sin\left(\alpha - \frac{\phi}{2}\right), \tag{32}$$

$$Z_{\text{imag}} = -\frac{l}{2(r_2 - r_1)k\omega\varepsilon_0\pi}\frac{\sqrt{D_3^2 + D_4^2}}{\sqrt{D_1^2 + D_2^2}}\cos\left(\alpha - \frac{\phi}{2}\right). \tag{33}$$

Note that if the value of D_3 becomes negative, the value of α in Eq. (B6) should be chosen such that $\pi/2 < \alpha < 3\pi/2$.

C. Overall impedance and rf voltage between the two electrodes

To determine the overall impedance between the two electrodes we need to include three components: (i) the sheath impedance at plate A, (ii) the bulk plasma impedance, and (iii) the sheath impedance at plate B. For an asymmetrically driven, parallel plate rf discharge (nonequal area plates) the sheath equations for plate B will be identical to those for plate A, except that the harmonics of the current density considered for calculation at plate A will be multiplied by a factor $b = A_A/A_B$, where A_A and A_B are the cross-sectional areas of plates A and B, respectively. The sheath voltage on plate B will be similar to that of plate A but shifted by a phase angle π. We let $V_{Ak}(\omega t)$ and $V_{Bk}(\omega t)$ be the kth harmonic voltages on plates A and B, respectively, with respect to the plasma; then from Eq. (5) we can write

$$V_{Ak}(\omega t)=\overline{V}_{Ak}\cos(k\omega t), \tag{34}$$

$$V_{Bk}(\omega t)=\overline{V}_{Bk}\cos[k(\omega t+\pi)]=(-1)^k\overline{V}_{Bk}\cos(k\omega t) \tag{35}$$

where $\overline{V}_{Ak}$ and $\overline{V}_{Bk}$ are the amplitudes of the kth harmonic sheath voltage at plates A and B, respectively, given by Eq. (7). Since the phase direction of $V_{Bk}(\omega t)$ is opposite to $V_{Ak}(\omega t)$ and the sheath capacitances are directly related to the sheath voltages, it can be seen from Eqs. (9), (34), and (35) that the equation for the equivalent sheath capacitance (in farad) for two sheaths is

$$C_{es\ k}=\frac{\overline{I_k}}{k\omega\{\overline{V}_{Ak}-(-1)^k\overline{V}_{Bk}\}}, \tag{36}$$

where $\overline{I_k}$ is the amplitude of the kth harmonic rf current (in amperes). The kth harmonic equivalent sheath resistance for the two sheaths (in ohms) can be written as

$$r_{es\ k}=\frac{1}{A_AG_{Ak}}+\frac{1}{A_BG_{Bk}}. \tag{37}$$

Here G_{Ak} and G_{Bk} are the kth harmonic sheath conductances (mho/m^2) of plates A and B, respectively, given by Eq. (19). From Eqs. (19) and (37) and using $\overline{J_{kB}}=b\overline{J_{kA}}$ we obtain

$$r_{esk}=\frac{3\overline{J_{kA}^2}m\Gamma_s}{4k^2e^3\omega^2T_e\varepsilon_0n_0^3A_A}(1+b^3), \tag{38}$$

where $\overline{J_{kA}}$ and $\overline{J_{kB}}$ are the amplitudes of the kth harmonic current density at plate A and plate B, respectively. Now, from Eqs. (31), (36), and (38) and using $\overline{I_k}=A_A\overline{J_{kA}}$ we obtain the kth harmonic overall impedance (in ohms) between the two plates as

$$Z_{ok}=\left[Z_{\text{real}}+\frac{3\overline{I_k^2}m\Gamma_s}{4k^2e^3\omega^2T_e\varepsilon_0n_0^3A_A^3}(1+b^3)\right]+j\left[Z_{\text{imag}}-\frac{\{\overline{V}_{Ak}-(-1)^k\overline{V}_{Bk}\}}{\overline{I_k}}\right]. \tag{39}$$

For a symmetrical discharge, $b=1$ and $\overline{V}_{Ak}=\overline{V}_{Bk}$. Thus replacing $\overline{V}_{Ak}$ and $\overline{V}_{Bk}$ by $\overline{V}_k$, and A_A, by A we can rewrite Eq. (39) for a symmetrical discharge as

$$Z_{ok}=\left[Z_{\text{real}}+\frac{3\overline{I_k^2}m\Gamma_s}{2k^2e^3\omega^2T_e\varepsilon_0n_0^3A^3}\right]+j\left[Z_{\text{imag}}-\{1-(-1)^k\}\frac{\overline{V_k}}{\overline{I_k}}\right]. \tag{40}$$

The overall kth harmonic rf voltage at the powered electrode with respect to the ground can be obtained as

$$\overline{V}_{\text{rf}k}=\overline{I_k}Z_{ok}, \tag{41}$$

where Z_{ok} is the kth harmonic overall rf impedance given by Eqs. (39) or (40).

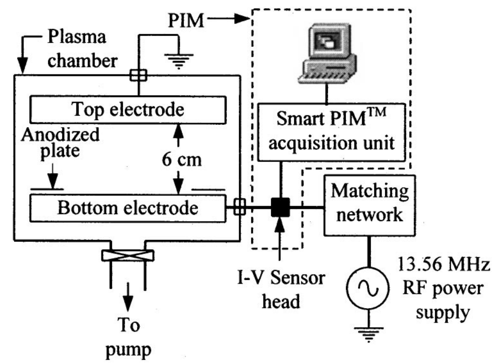

FIG. 3. A schematic diagram of the experimental equipment including the PIM.

It is important to note here that in the Lieberman model there is no even harmonic overall rf voltage and hence no even harmonic impedance. This was always a problem with this model, as our measurements (see Sec. IV) have always observed even harmonic components. We have found that the even harmonic components of rf impedance never become zero in the present model. This is because the sheath resistance associated with the stochastic heating in the two sheaths and the bulk plasma impedance are always present, even for a symmetrical discharge. From Eq. (40) we see that in a symmetrical discharge only the sheath capacitance effect is diminished in the overall impedance.

III. EXPERIMENT

The experimental apparatus is a capacitively coupled parallel plate reactor coupled with a plasma impedance monitor (PIM) shown by Fig. 3. It consists of two water-cooled circular aluminum electrodes separated by a 6 cm gap. The diameter of the upper electrode is 28.5 cm whereas the lower electrode is 24 cm in diameter. A Pyrex cylinder seals the whole plasma chamber. For reactive ion etch (RIE) operation the upper electrode is grounded and the lower electrode is supplied by a 13.56 MHz rf generator. A replaceable hollow circular shaped anodized aluminum plate is placed above the lower electrode which provides a variable effective area for the powered electrode. The word ''effective'' is used here because the anodized plate acts as an insulator and thus only the exposed part of the powered electrode comes in contact with the plasma. An impedance matching circuit is placed between the rf generator and the powered electrode to minimize the reflected power from the plasma chamber. A mass flow controller unit controls the flow of inlet gases into the chamber where a rotary pump maintains the necessary vacuum in the chamber.

The PIM (shown by the dotted line in Fig. 3) comprises a Scientific Systems Smart PIM™ unit interfaced to a personal computer. The Smart PIM™ is a microprocessor-based electronic system for measuring rf plasmas.[21,25–27] The current–voltage ($I-V$) sensor located between the matching network and the driven electrode of the plasma reactor measures current and voltage signals that are proportional to the plasma rf current and voltage. The signal is fed via the $I-V$ cable to the Smart PIM™ acquisition unit. Microprocessor

TABLE I. Harmonic components of rf current recorded in the experiment for different effective diameter settings of the powered electrode.

Diameter of the powered electrode, D_1 (cm)	I_1 (A)	I_2 (A)	I_3 (A)	I_4 (A)	I_5 (A)
16	9.0797	0.1895	0.1627	0.1062	0.0399
18	9.9394	0.2011	0.1841	0.0491	0.0375
20	9.4951	0.1836	0.1755	0.0557	0.0338

based analysis routines operate on the acquired signals to yield the Fourier components of the fundamental and the first four harmonic components. The phase angle between the harmonic components is also computed. The fundamental and the first four harmonic components of the current and voltage signals and the phase angle between the respective components are transferred to the microcomputer via an interface cable for display and further analysis using the Scientific Systems Windows™ based software, PIMSoft™. The resolutions of this equipment for rf voltage, current, and phase are ±1 V, ±1 mA and ±0.01°, respectively.[25]

The plasma system described above was run in RIE mode with Ar gas at 180 W rf power, 30 mTorr chamber pressure, and 4.35 sccm gas flow rate. The fundamental and the harmonic components (up to the fifth harmonic, where fundamental frequency = 13.56 MHz) of rf current, voltage, and impedance were recorded using the PIM. The experiment was repeated for the same operating condition but different effective diameters of the powered electrode. The results obtained from the experiments were compared with the modeled parameters.

IV. RESULTS AND DISCUSSIONS

Using the fundamental and the first four harmonic components of the rf current measured in the experiments (shown by Table I) as parameters (other harmonics of rf current are assumed to be zero) the first five harmonics of rf voltage and impedance were calculated. Since there was no facility in our laboratory to experimentally measure the three characteristic plasma parameters, i.e., the plasma density n_0, electron temperature T_e, and the electron-neutral collision frequency ν_m, typical values of these parameters (shown in Table II) were used in the calculations. These three parameters depend strongly upon the operating condition of the plasma (i.e., discharge power, operating pressure, the gas flow rate, and the geometry of the plasma chamber) and change drastically for a small change in one of these. For this reason it is very difficult to assume the exact values of these parameters and hence the calculated values of the different parameters may vary significantly in absolute value from the measured values. In this work we used typical values of these three plasma characteristics to elucidate trends in the data such as the relative contributions of each harmonic component of rf voltage and impedance. To analyze the trends in the data the measured and the calculated values of the rf voltage and impedance were normalized with respect to their fundamental components and plotted on the same graph.

TABLE II. Typical values of three plasma characteristics used for calculations.

n_0	T_e	ν_m
1×10^{12} cm^{-3}	3.5 V	2×10^{7} s^{-1}

Figures 4 and 5 show the comparison between the measured and the calculated values of the rf voltage and impedance, respectively, while the diameter of the powered electrode is set to 18 and 20 cm, respectively. It is clear from the figures that the relative magnitudes of both the rf voltage and impedance harmonics calculated using the present model follow qualitatively the values measured in the experiment. In the modeling we saw that the plasma equations are nonlinear in behavior and that they depend on the aforementioned three plasma characteristics (n_0, T_e, and ν_m) in a strong nonlinear fashion. This has a major impact on why the calculated rf voltage and impedance harmonics do not match exactly with the measured values but follow the trend of relative magnitudes of each of the harmonic components. To obtain improved results one should use the exact values of the above

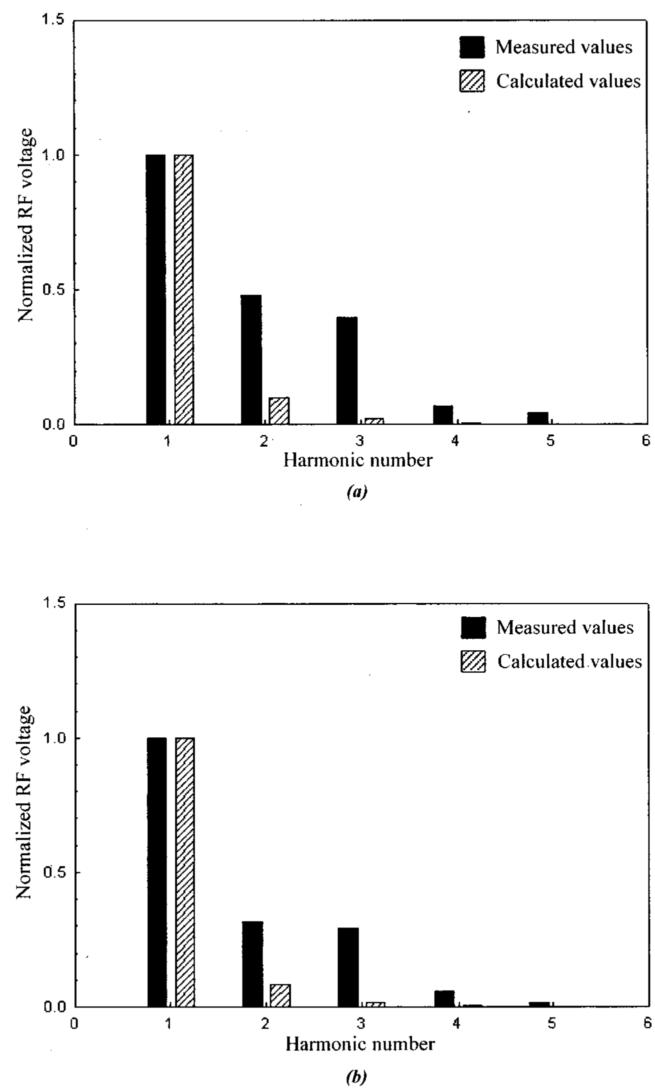

FIG. 4. Normalized rf voltage as a function of the harmonic number for two different effective diameters of the powered electrode, D_1; (a) $D_1 = 18$ cm and (b) $D_1 = 20$ cm.

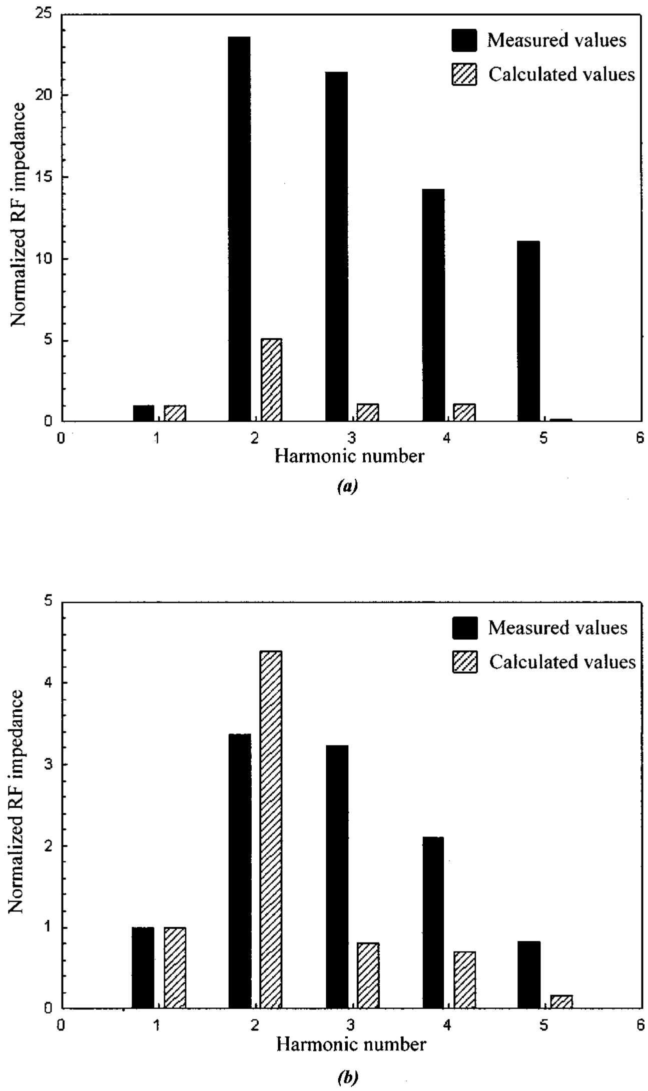

FIG. 5. Normalized rf impedance as a function of the harmonic number for two different effective diameters of the powered electrode, D_1; (a) $D_1 = 18$ cm and (b) $D_1 = 20$ cm.

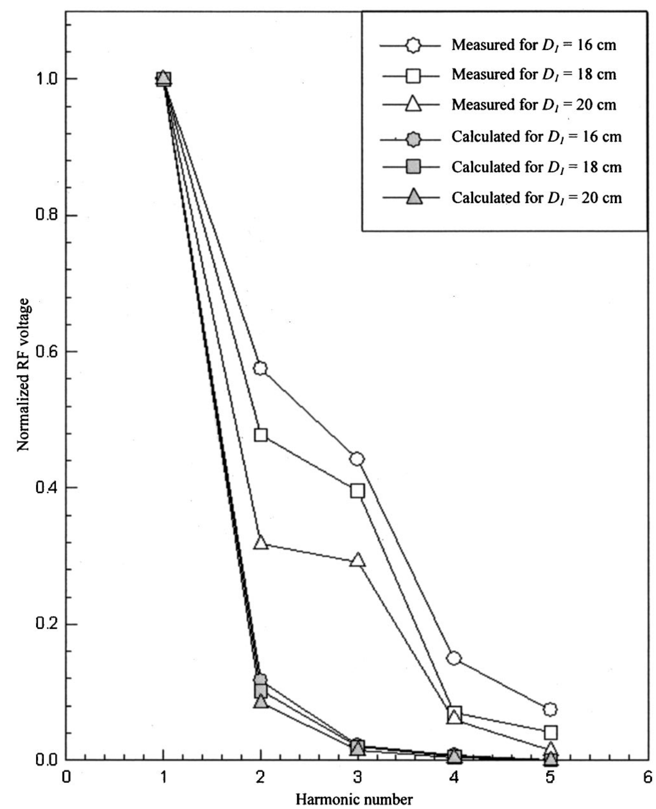

FIG. 6. Comparison of calculated and measured values of normalized rf voltage for the effective diameter of the powered electrode, $D_1 = 16$, 18, and 20 cm, respectively.

three plasma characteristic parameters, if available.

Figures 6 and 7 show a comparison between the calculated and measured values of rf voltage and impedance harmonics, respectively, for three different diameter settings of the powered electrode. From these figures we see again that the overall qualitative trends are similar for measured and calculated values. But the values of both rf voltage and impedance harmonics move to lower values as the effective diameter of the powered electrode, D_1, increases. This can be explained in the following way. We saw in the modeling section [see Eq. (40)] that there is no sheath capacitance effect on the even harmonic components of rf impedance for a symmetric discharge. That means that the harmonic phenomenon is reduced as the asymmetry of the system is reduced. In other words, the fundamental component will be more prominent in less asymmetric systems. When the harmonic components are normalized with respect to the fundamental, they will be of lower value than those of more asymmetric systems. Now, an increase in the diameter of the powered electrode reduces the asymmetry of the system, as the diameter of the grounded electrode is fixed (28.5 cm). This is the main reason why the normalized curves of the rf voltage and impedance harmonics shift downward for higher D_1.

V. CONCLUSIONS

We present an analytical solution for a high voltage, collisionless, capacitive rf sheath driven by a nonsinusoidal rf current. We obtain analytical expressions for some important sheath parameters, i.e., the time-average ion and electron densities, electrical field and electric potential within the sheath, nonlinear oscillation motion of the electron sheath boundary, the effective sheath impedance, etc. The Lieberman model[17] for the sheath parameters is also obtainable from the present model if we assume that all the harmonic components of the rf current, except the fundamental, equal zero.

We have determined the overall rf voltage and impedance for each of the harmonic frequencies considering an asymmetric discharge. We also obtained the equation for the same quantities for a symmetric discharge. In the calculation of the overall impedance we included the bulk plasma impedance together with the two sheath impedances while the bulk impedance was not included in the Lieberman model. We have found that the even harmonic components of rf voltage and impedance are always present in this model (even for a symmetric discharge) whereas there is no even harmonic component in the Lieberman model. This is be-

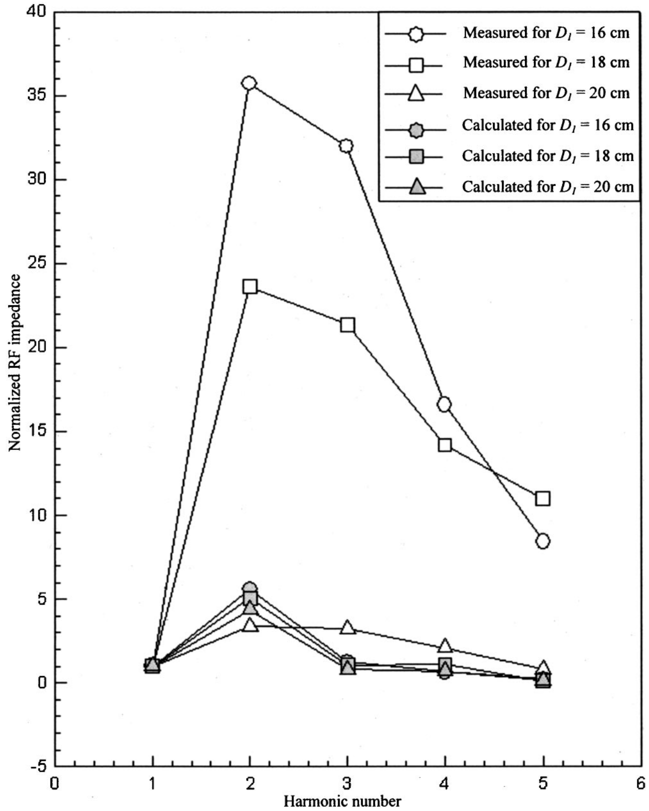

FIG. 7. Comparison of calculated and measured values of normalized rf impedance for the effective diameter of the powered electrode, $D_1 = 16$, 18, and 20 cm, respectively.

cause the sheath resistance effect, associated with the stochastic heating in the two sheaths, and the bulk plasma impedance never become zero. Only the sheath capacitance effect is diminished at even harmonic frequencies when the discharge is symmetric.

It is shown that the relative magnitudes of rf voltage and impedance harmonics determined by the present model follow qualitatively the values measured experimentally, as they follow the trend of the relative magnitudes of each of the harmonic components. The values of the normalized rf voltage and impedance harmonics assume lower values both for calculated and measured quantities as the asymmetry of the plasma chamber decreases. This is possibly because the harmonic phenomenon decreases with a decrease of the asymmetry of the chamber.

ACKNOWLEDGMENTS

The authors wish to thank Plasma Ireland Ltd. for the provision of the Plasma Impedance Monitor (Smart PIM™). The authors would also like to thank Dr. Miles Turner, School of Physical Science, Dublin City University, Dublin, Ireland for many useful discussions about this work. The support of the Enterprise Ireland Strategic Research Grant Scheme is gratefully acknowledged.

APPENDIX A: DERIVATION OF PRINCIPAL SHEATH PARAMETERS

The relation between the ion density n_i and the time-average potential $\overline{\Phi}$ within the sheath is given by[17]

$$n_i = n_0\left(1 - \frac{2\overline{\Phi}}{T_e}\right)^{-(1/2)}, \tag{A1}$$

where n_0 and T_e are the plasma density at $x=0$ and the electron temperature, respectively. Here $\overline{\Phi}$ and n_i are functions of x. The time-average electric field $\overline{E}(x)$ and potential $\overline{\Phi}(x)$ can be expressed as

$$\frac{d\overline{E}}{dx} = \frac{e}{\varepsilon_0}[n_i(x) - \overline{n_e}(x)], \tag{A2}$$

$$\frac{d\overline{\Phi}}{dx} = -\overline{E}, \tag{A3}$$

where e and ε_0 are the ion charge and the permittivity of free space, respectively. The time-average electron density $\overline{n_e}$ within the sheath can be given as[17]

$$\overline{n_e}(x) = \left(1 - \frac{\varphi}{\pi}\right) n_i(x), \tag{A4}$$

where $2\varphi(x) = 2\omega t$ is the phase interval during which $s(t) < x$; $s(t)$ is the distance from the ion sheath boundary at $x=0$ to the electron sheath edge. The time-average electron density $\overline{n_e}(x)$ is shown as a dashed line in Fig. 1.

Equating the displacement current given by Eq. (1) to the conduction current at the electron sheath boundary, we obtain the equation for the electron sheath motion as

$$-en_i(s)\frac{ds}{dt} = -\sum_{p=1}^{N} \overline{J_p}\sin(p\omega t). \tag{A5}$$

The time varing electric field within the sheath is given by[17]

$$E = \frac{e}{\varepsilon_0}\int_s^x n_i(\xi)d\xi, \quad s(t)<x=0, \quad s(t)>x. \tag{A6}$$

Integrating Eq. (A5) we obtain

$$\frac{e}{\varepsilon_0}\int_0^\infty n_i(\xi)d\xi = \sum_{p=1}^{N}\frac{\overline{J_p}}{p\omega\varepsilon_0}[1-\cos(p\omega t)]. \tag{A7}$$

Putting $s=x$ at $\omega t = \varphi$ in Eq. (A7) we have

$$\frac{e}{\varepsilon_0}\int_0^x n_i(\xi)d\xi = \sum_{p=1}^{N}\frac{\overline{J_p}}{p\omega\varepsilon_0}[1-\cos(p\varphi)]. \tag{A8}$$

Subtracting Eq. (A7) from Eq. (A8) we obtain

$$\frac{e}{\varepsilon_0}\int_s^x n_i(\xi)d\xi = \sum_{p=1}^{N}\frac{\overline{J_p}}{p\omega\varepsilon_0}[\cos(p\omega t)-\cos(p\varphi)]. \tag{A9}$$

Equating Eqs. (A6) and (A9) we obtain

$$E(x,\omega t) = \sum_{p=1}^{N}\frac{\overline{J_p}}{p\omega\varepsilon_0}[\cos(p\omega t)-\cos(p\sigma)],$$

$$s(t)<x=0, \quad s(t)>x. \tag{A10}$$

We note that $s(t)=x$ at $\omega t=\varphi$ and $s(t)<x$ when $-\varphi<\omega t<\varphi$. Taking the time-average we obtain from Eq. (A10)

$$\overline{E}(x)=\frac{1}{2\pi}\int_{-\varphi}^{\varphi}E(x,\omega t)d\omega t. \tag{A11}$$

Inserting Eq. (A10) into Eq. (A11) and integrating we obtain

$$\overline{E}(x)=\sum_{p=1}^{N}\frac{\overline{J_p}}{p\omega\varepsilon_0\pi}\left[\frac{1}{p}\sin(p\varphi)-\varphi\cos(p\varphi)\right]. \tag{A12}$$

Inserting Eq. (A12) into Eq. (A3) we obtain

$$\frac{d\overline{\Phi}}{dx}=-\sum_{p=1}^{N}\frac{\overline{J_p}}{p\omega\varepsilon_0\pi}\left[\frac{1}{p}\sin(p\varphi)-\varphi\cos(p\varphi)\right]. \tag{A13}$$

Inserting Eq. (A1) into Eq. (A5) with $s(t)=x$, $\omega t=\varphi$, we obtain

$$\frac{d\varphi}{dx}=\frac{e\omega n_0(1-2\overline{\Phi}/T_e)^{-(1/2)}}{\Sigma_{p=1}^{N}\overline{J_p}\sin(p\varphi)}. \tag{A14}$$

Dividing Eq. (A13) by Eq. (A14) and integrating we obtain the equation for the time-average potential as

$$\frac{\overline{\Phi}}{T_e}=\frac{1}{2}-\frac{1}{2}\left[1-\frac{1}{e\omega^2T_e\varepsilon_0\pi n_0}\left\{\sum_{p=1}^{N}\sum_{\substack{q=1\\q\neq p}}^{N}\frac{\overline{J_p}J_q}{p}\right.\right.$$
$$\times\left(\frac{2p+q}{2p(p+q)^2}\sin(p+q)\varphi-\frac{2p-q}{2p(p-q)^2}\right.$$
$$\times\sin(p-q)\varphi-\frac{1}{2(p+q)}\varphi\cos(p+q)\varphi$$
$$\left.+\frac{1}{2(p-q)}\varphi\cos(p-q)\varphi+\sum_{p=1}^{N}\frac{\overline{J_p^2}}{p}\right.$$
$$\left.\times\left(\frac{3}{8p^2}\sin(2p\varphi)-\frac{\varphi}{4p}\cos(2p\varphi)-\frac{\varphi}{2p}\right)^2, \tag{A15}$$

and from Eq. (A15), using $\overline{V}=-\overline{\Phi}(\varphi=\pi)$ the net dc voltage across the sheath can be given by

$$\frac{\overline{V}}{T_e}=-\frac{1}{2}+\frac{1}{2}\left[1+\frac{1}{2e\omega^2T_e\varepsilon_0n_0}\left\{\sum_{p=1}^{N}\sum_{\substack{q=1\\q\neq p}}^{N}\frac{\overline{J_p}\overline{J_q}}{p}\right.\right.$$
$$\times\left(\frac{1}{(p+q)}\cos(p+q)\pi-\frac{1}{(p-q)}\cos(p-q)\pi\right)$$
$$\left.\left.+\frac{3}{2}\sum_{p=1}^{N}\frac{\overline{J_p^2}}{p^2}\right\}\right]^2. \tag{A16}$$

Inserting Eq. (A15) into Eq. (A16) and integrating with $\varphi=0$ at $x=0$ we have

$$e\omega n_0x=\sum_{p=1}^{N}\overline{J_p}\int_0^{\varphi}\sin(p\varphi)d\varphi-\frac{1}{e\omega^2T_e\varepsilon_0\pi n_0}\left[\sum_{p=1}^{N}\sum_{\substack{q=1\\q\neq p}}^{N}\sum_{r=1}^{N}\frac{\overline{J_p}\overline{J_q}\overline{J_r}}{p}\int_0^{\varphi}\left\{\frac{2p+q}{2p(p+q)^2}\sin(p+q)\varphi-\frac{2p-q}{2p(p-q)^2}\right.\right.$$
$$\left.\times\sin(p-q)\varphi-\frac{1}{2(p+q)}\varphi\cos(P+q)\varphi+\frac{1}{2(p-q)}\varphi\cos(p-q)\varphi\right\}\sin(r\varphi)d\varphi+\sum_{p=1}^{N}\sum_{r=1}^{N}\frac{\overline{J_p^2}\overline{J_r}}{p}$$
$$\left.\times\int_0^{\varphi}\left\{\frac{3}{8p^2}\sin(2p\varphi)-\frac{\varphi}{4p}\cos(2p\varphi)-\frac{\varphi}{2p}\right\}\sin(r\varphi)d\varphi\right]. \tag{A17}$$

Putting $x=s(t)$ and $\varphi=\omega t$ in Eq. (A17), we obtain the nonlinear motion of the electron sheath. Again using Eq. (A17) and putting $x=s_m$ at $\varphi=\pi$ we can calculate the ion sheath thickness s_m. From Eqs. (A1) and (A15) we obtain the equation for ion density as

$$n_i=n_0\left[1-\frac{1}{e\omega^2T_e\varepsilon_0\pi n_0}\left\{\sum_{p=1}^{N}\sum_{\substack{q=1\\q\neq q}}^{N}\frac{\overline{J_p}\overline{J_q}}{p}\left(\frac{2p+q}{2p(p+q)^2}\sin(p+q)\varphi-\frac{2p-q}{2p(p-q)^2}\sin(p-q)\varphi-\frac{1}{2(p+q)}\varphi\cos(p+q)\varphi\right.\right.\right.$$
$$\left.\left.\left.+\frac{1}{2(p-q)}\varphi\cos(p-q)\varphi\right)+\sum_{p=1}^{N}\frac{\overline{J_p^2}}{p}\left(\frac{3}{8p^2}\sin(2p\sigma)-\frac{\varphi}{4p}\cos(2p\varphi)-\frac{\varphi}{2p}\right)\right\}\right]^{-1}. \tag{A18}$$

APPENDIX B: COEFFICIENTS USED IN THE CALCULATION OF *k*th HARMONIC BULK IMPEDANCE [EQ. (30)]

$$\phi=\tan^{-1}\left(\frac{\nu_m}{k\omega}\right), \tag{B1}$$

$$D_1=eR_1\left(\frac{n_{01}}{k\omega\varepsilon_0 m}\right)^{1/2}(k^2\omega^2+\nu_m^2)^{-(1/4)}\cos(\phi/2), \tag{B2}$$

$$D_2=eR_1\left(\frac{n_{01}}{k\omega\varepsilon_0 m}\right)^{1/2}(k^2\omega^2+\nu_m^2)^{-(1/4)}\sin(\phi/2), \tag{B3}$$

$$D_3=\frac{1}{2}\ln \times\left[\frac{\{(R_2-D_1)(R_1+D_1)+D_2^2\}^2+\{D_2(R_2-R_1-2D_1)\}^2}{\{(R_2+D_1)(R_1-D_1)+D_2^2\}^2+\{D_2(R_1-R_2-2D_1)\}^2}\right], \tag{B4}$$

$$D_4=\tan^{-1}\frac{D_2(R_2-R_1-2D_1)}{(R_2-D_1)(R_1+D_1)+D_2^2} -\tan^{-1}\frac{D_2(R_1-R_2-2D_1)}{(R_2+D_1)(R_1-D_1)+D_2^2}, \tag{B5}$$

$$\alpha=\tan^{-1}\frac{D_4}{D_3}. \tag{B6}$$

[1] D. M. Manos and D. L. Flamm, *Plasma Etching* (Academic, New York, 1989).
[2] V. A. Godyak, Sov. J. Plasma Phys. **2**, 78 (1976).
[3] V. A. Godyak and O. A. Popov, Sov. J. Plasma Phys. **5**, 227 (1979).
[4] H. R. Koenig and L. I. Maissel, IBM J. Res. Dev. **14**, 168 (1970).
[5] J. M. Keller and W. B. Pennebaker, IBM J. Res. Dev. **23**, 3 (1979).
[6] W. B. Pennebaker, IBM J. Res. Dev. **23**, 16 (1979).
[7] V. A. Godyak and Z. K. Ganna, Sov. J. Plasma Phys. **6**, 372 (1980).
[8] V. Vahedi, C. K. Birdsall, M. A. Lieberman, G. DiPeso, and T. D. Rognlien, Plasma Sources Sci. Technol. **2**, 273 (1993).
[9] M. J. Grapperhaus and M. J. Kushner, J. Appl. Phys. **81**, 569 (1997).
[10] P. A. Miller and M. E. Riley, J. Appl. Phys. **82**, 3689 (1997).
[11] D. Vender and R. W. Boswell, J. Vac. Sci. Technol. A **10**, 1331 (1992).
[12] V. A. Godyak and N. Sternberg, IEEE Trans. Plasma Sci. **18**, 159 (1990).
[13] N. Sternberg and V. A. Godyak, IEEE Trans. Magn. **30**, 3100 (1994).
[14] K. Börnig, Appl. Phys. Lett. **60**, 1553 (1992).
[15] A. Metze, D. W. Ernie, and H. J. Oskam, J. Appl. Phys. **60**, 3081 (1986).
[16] V. A. Godyak and N. Sternberg, Phys. Rev. A **42**, 2299 (1990).
[17] M. A. Lieberman, IEEE Trans. Plasma Sci. **16**, 638 (1988).
[18] M. Chandhok and J. W. Grizzle, IEEE Trans. Plasma Sci. **26**, 181 (1998).
[19] V. A. Godyak, R. B. Piejak, and B. M. Alexandrovich, IEEE Trans. Plasma Sci. **19**, 660 (1991).
[20] H. Kawata, T. Kubo, and K. Murata, Jpn. J. Appl. Phys., Part 1 **33**, 4365 (1994).
[21] M. N. A. Dewan, P. J. McNally, and P. A. F. Herbert, Proceedings of the International Conference on Advances in Materials & Processing Technologies, (AMPT ’99) II, edited by M. S. J. Hashmi 939 (DCU Press, Dublin, 1999), p. 939.
[22] M. A. Lieberman and A. J. Lichtenberg, *Principles of Plasma Discharges and Materials Processing* (Wiley, New York, 1994).
[23] A. Beiser, *Concept of Modern Physics*, 4th ed. (McGraw-Hill, New York, 1987).
[24] V. A. Godyak, R. B. Piejak, and B. M. Alexandrovich, Plasma Sources Sci. Technol. **1**, 36 (1992).
[25] Internet: http://www.scisys.com (Scientific Systems Ltd., Dublin, Ireland, 2000).
[26] Scientific Systems Ltd., Smart PIM™ installation and software manual (Scientific Systems Ltd., Dublin, Ireland, 1997).
[27] O. A. Popov and V. A. Godyak, J. Appl. Phys. **57**, 53 (1985).